POLITECNICO DI TORINO
Repository ISTITUZIONALE

Non-destructive evaluation of ductile-porous versus brittle 3D printed vascular networks in self-healing concrete

Original
Non-destructive evaluation of ductile-porous versus brittle 3D printed vascular networks in self-healing concrete / Shields, Y., Tsangouri, E., Riordan, C., De Nardi, C., Godinho, J.R.A., Ticho, O., Antonaci, P., Palmer, D., Al-Tabbaa, A., Jefferson, T., De Belie, N., Van Tittelboom, K.. - In: CEMENT & CONCRETE COMPOSITES. - ISSN 0958-9465. - STAMPA. - 145:(2024), pp. 1-10. [10.1016/j.cemconcomp.2023.105333]

Availability:
This version is available at: 11583/2986163 since: 2024-02-22T14:07:52Z

Publisher:
Elsevier

Published
DOI:10.1016/j.cemconcomp.2023.105333

Terms of use:

This article is made available under terms and conditions as specified in the corresponding bibliographic description in the repository

Publisher copyright

(Article begins on next page)

17 October 2026

Please cite this article as: Y. Shields, E. Tsangouri, C. Riordan, C. De Nardi, Jose.Ricardo.Assunçã. Godinho, P. Antonaci, D. Palmer, A. Al-Tabbaa, T. Jefferson, N. De Belie, K. Van Tittelboom, Non-destructive evaluation of ductile-porous versus brittle 3D printed vascular networks in self-healing concrete, *Cement and Concrete Composites* (2023), doi: https://doi.org/10.1016/j.cemconcomp.2023.105333.

Non-destructive evaluation of ductile-porous versus brittle 3D printed vascular networks in self-healing concrete

Yasmina Shields[1], Eleni Tsangouri[2], Claire Riordan[3,4], Cristina De Nardi[5], Jose Ricardo Assunção Godinho[6], Paola Antonaci[7], Dave Palmer[3], Abir Al-Tabbaa[4], Tony Jefferson[5], Nele De Belie[1], and Kim Van Tittelboom[1]

[1]Magnel-Vandepitte Laboratory, Department of Structural Engineering and Building Materials, Faculty of Engineering and Architecture, Ghent University, Ghent, Belgium

[2]Dept. Mechanics of Materials and Constructions (MeMC), Vrije Universiteit Brussel (VUB), Brussels, Belgium

[3]Micropore Technologies Ltd, Redcar, UK

[4]Department of Engineering, University of Cambridge, Cambridge, UK

[5]School of Engineering, Cardiff University, Wales, UK

[6]Helmholtz-Zentrum Dresden-Rossendorf, Helmholtz Institute Freiberg for Resource Technology, Chemnitzer Straße 40, 09599, Freiberg, Germany.

[7]Department of Structural, Geotechnical and Building Engineering, Politecnico di Torino, Turin, Italy

Keywords: vascular networks, self-healing concrete, 3D printing, non-destructive testing

1. Abstract

Additive manufacturing (AM) can produce complex vascular network configurations, yet limited testing has been done to characterize the damage and healing behavior of concrete with embedded networks for self-healing. In this study, different AM methods and network wall materials were used to produce vascular networks for self-healing concrete prisms, where their load-response behavior, healing efficiency and microstructure were evaluated using non-destructive techniques: acoustic emission (AE), ultrasonic pulse velocity (UPV), digital image correlation (DIC), and X -ray computed tomography (CT). The types of healing agent release mechanisms that were studied include a ductile-porous network that supplies fluid from its pores and a brittle network that fractures under load to release fluid. DIC coupled with AE verified debonding of ductile-porous networks from the cementitious matrix, and was able to track damage progression as well as healing for all networks with load regains up to 56% and stiffness regains up to 91% using polyurethane.

2. Introduction

A variety of self-healing mechanisms for concrete applications have the potential to reduce the environmental impact of concrete structures and enhance their durability by autonomously or autogenously healing cracks [1]. Vascular networks have unique advantages over other healing mechanisms in that they are capable of having multiple healing cycles, delivering a healing agent on an as-needed basis and enhancing healing due to their pressurization capabilities. Brittle networks are the most common type of network being used in self-healing vascular network systems for concrete research. The wall material is either inherently brittle or the networks are designed with a rough surface to provide adequate bonding to the cementitious matrix and with weak tensile properties, so that when a crack forms in the concrete matrix, the network breaks along with it.

Vascular self-healing concrete research thus far includes studies on hollow channels/networks made from sacrificial materials (subtractive manufacturing) [2]–[4], as well as brittle networks made from glass [5]–[7] or fabricated via 3D printing (additive manufacturing) [8]–[12]. Subtractive manufacturing introduces additional voids into the concrete element that could weaken its mechanical properties, and nonlinear, complex

configurations may also be difficult to practically install onsite. Brittle networks may not be conducive for practical applications, as often these networks are too brittle to survive realistic concrete casting methods. This can be mitigated by using a self-consolidating mix design, however this results in an added cost and does not solve the problem of handling a long, brittle network onsite.

3D printing brittle vasculature takes significantly more time to manufacture compared to traditional extrusion or injection processes (hours vs. seconds), and the risk of network breakage during on-site handling, installation, and concrete pouring is high. Additionally, the size limitations of 3D printers restrict vascular channels to smaller lengths, which in turn require connections and added labor costs, as well as require additional support material to produce. To overcome the disadvantages that exist for fabricating, installing, and using brittle vasculature, the main motivation for this work is to present a new 3D printed ductile-porous system that overcomes these issues, and that is studied in comparison with a traditional 3D-printed brittle network. Instead of fracturing with the surrounding cementitious matrix, the ductile-porous network would remain intact and detach from the matrix to release a healing agent through pores included throughout the network wall.

Fused deposition modelling (FDM) is the most widely used technique of 3D printing, which works by extruding a melted thermoplastic polymeric filament through a nozzle layer-by-layer to fabricate a part. A brittle network made using FDM should be printed perpendicularly to the build plate so that the printed layers are parallel to the direction of loading. By printing in this direction, the network will be weaker and will fail along the layer lines. Polylactic acid (PLA) and polyethylene terephthalate glycol (PET-G) filaments have been used in previous vascular designs for this purpose due to their brittle properties [8]. In order to make a printed part more ductile, either the printing direction will need to be horizontal to the build plate, or a ductile polymeric filament material can be used. Thermoplastic elastomers (TPE) are ductile filaments that contain a combination of rigid plastic and rubber properties; types of TPEs include polypropylene (PP), thermoplastic co-polyester (TPC), and thermoplastic polyurethane (TPU). In this study, a brittle network was produced via FDM using PLA filament and compared to two types of ductile-porous networks.

An additional 3D printing technique, stereolithography (SLA), or vat polymerization, is used for the first time to fabricate self-healing vascular networks in concrete. It works by using a low-powered laser to harden a photo-sensitive liquid resin in a layer-by-layer fashion. Objects are inversely printed through the submerging of the build plate into a resin layer or resin vat, depending on the material used. Post-printing, objects are washed in solvent to remove excess resin before a dual-thermal and UV curing step. This curing step will alter the final mechanical characteristics of the printed objects. Commercially available acrylate resins are often used, all with varying levels of ductility and strength. This technique was chosen as it can achieve higher dimensional accuracies compared to FDM and will thus have less surface roughness [13], which is needed for a ductile-porous network design that will debond from the surrounding cementitious matrix.

The combination of acoustic emission (AE), digital image correlation (DIC), X-ray computed tomography (CT) and ultrasonic pulse velocity (UPV) measurements have been well established as monitoring techniques for assessing the damage and healing evolution of laboratory scale self-healing concrete elements [14]–[17], and they were used here to monitor crack opening and healing in self-healing concrete, and to critically examine mechanical performance. AE allows for damage characterization by analyzing the transient waves that are generated by crack propagation within the cementitious matrix, which are recorded by sensors

placed at the surface of the material or embedded within. DIC compares images of a sample during a test, and tracks the surface displacements of a speckle pattern applied to the surface. CT can be used to non-destructively observe and assess the internal microstructure of a material, and UPV gives an indication of crack filling after a healing agent has been supplied. The use of these multiple non-destructive techniques prior, during and following mechanical loading and self-healing was implemented in this study to provide a comprehensive assessment of damage and healing behavior.

3. Materials and methods

3.1. Concrete mix properties and configuration

Concrete beams with dimensions of 60 x 60 x 220 mm^3 were cast using the mix composition presented in Table 1; a triangular notch with a height of 3 mm was included at the bottom midspan of the beam to ensure that the crack forms at the center. The vascular networks had a 10 mm concrete cover and were fixed to the molds with a winged distribution piece (Figure 1), and sealed with silicone sealant. The mix used CEM I 52.5 N cement with a water to cement ratio of 0.45 and limestone filler with a particle size <125 µm. A maximum aggregate size of 8 mm was included so that aggregates would easily pass between the vascular channels and the walls of the mold. To improve workability, a superplasticizer was included in the mix design (Master Glenium 27 concentration of 20%, BASF, Belgium).

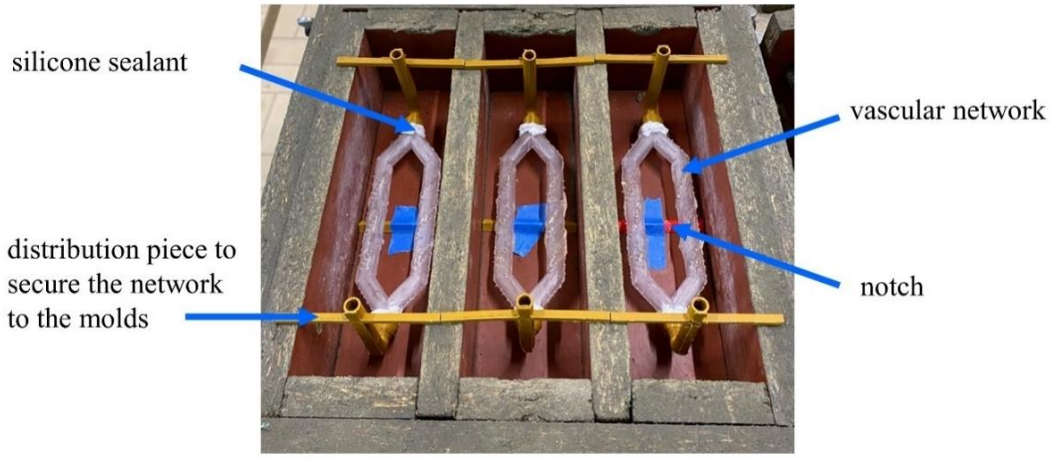

Figure 1. Concrete mold set-up.

Table 1. Concrete mix composition.

Components	Quantity (kg/m^3)
CEM I 52.5 N	341
Sand 0 - 4 mm	672
Gravel 2 - 8 mm	766
Limestone filler	182
Water	153
Superplasticizer	8.98

Concrete was prepared in a 50 L capacity vertical shaft mixer with a rotating pan (Eirich, Germany). After the dry components were mixed for 1 minute, water was added and mixing continued for 3 minutes. The superplasticizer was added 30 seconds after the water was

added. A first layer of fresh concrete was slowly added around the channels to ensure there were no voids beneath them, after which the remaining fresh concrete was added to the molds.

3.2. Samples with brittle and ductile-porous healing agent release mechanisms

Three different network types were developed: 1) ribbed brittle networks with PLA filament using FDM (B-PLA-FDM), 2) ductile-porous networks with polypropylene (PP) filament using FDM (DP-PP-FDM), and 3) ductile-porous networks with Flexible 80A resin (Formlabs, Somerville, Massachusetts, USA) made using SLA (DP-FLX-SLA). An additional reference series with no network embedded was also included. For each series a total of three samples were included. Sample designations for each network type are given in Table 2.

Table 2. Sample designations.

Series Name	Healing agent release mechanism	Network wall material	Printing method	Printing orientation
B-PLA-FDM	By network fracturing	Polylactic acid (PLA)	Fused deposition modelling (FDM)	Perpendicular to the build plate
DP-PP-FDM	Through debonding of the network and the included pores	Polypropylene (PP)	Fused deposition modelling (FDM)	Parallel to the build plate
DP-FLX-SLA	Through debonding of the network and the included pores	Formlabs Flexible 80A (FLX)	Stereolithography (SLA)	Parallel to the build plate

The geometric configuration of the networks was based on Murray's law (used in previous vascular self-healing concrete research [9], [17]), which minimizes the power required for fluid transport by relating the radii of the parent (r_p) and daughter (r_d) branches:

$$r_p^3 = r_{d1}^3 + r_{d2}^3 \quad \text{(Equation 1)}$$

For the cube law presented in Equation 1, Murray also determined the optimal branching angle to be 75° [18], which was implemented in this network design.

A ribbing pattern was introduced in the design of the brittle network channels to promote mechanical anchoring to the concrete, so that they are guaranteed to fracture upon crack formation in order to release the healing agent. Ribbing patterns were studied by De Nardi et al. in [8] in terms of mechanical bonding to concrete and likelihood of rupture at a desired crack opening; their recommendation of using spiral ribbing patterns with a 5 mm pitch was implemented in this design. The brittle networks in this study included a wall thickness of 1.2 mm to ensure the networks are watertight during concrete casting. An internal diameter of 7 mm was chosen for the daughter branches of all network types due to the limitations of the SLA printer.

For the ductile-porous network design, a staggered double spiral pattern of square pores with 1.5 mm openings was included to increase the chance of crack interception with at least one pore in case debonding would not occur. The printability of the SLA networks governed the design, as 1.5 mm pores were the smallest that could be printed without excessive post-processing steps. Extensive preliminary tests were carried out which informed the design of the SLA networks, which in addition to the pore sizes included the minimal wall thickness and internal diameter that could be feasibly printed. A wall thickness of 1.2 mm was used in order to be consistent with the permeability limitations of the brittle network fabrication. The pores were temporarily plugged by manually applying a layer of gelatin solution (approximately 1 mm thick) to prevent concrete infiltration during casting. Before supplying

the healing agent, hot water was flushed through the networks to dissolve the gelatin to allow the pores to be available to release the healing agent.

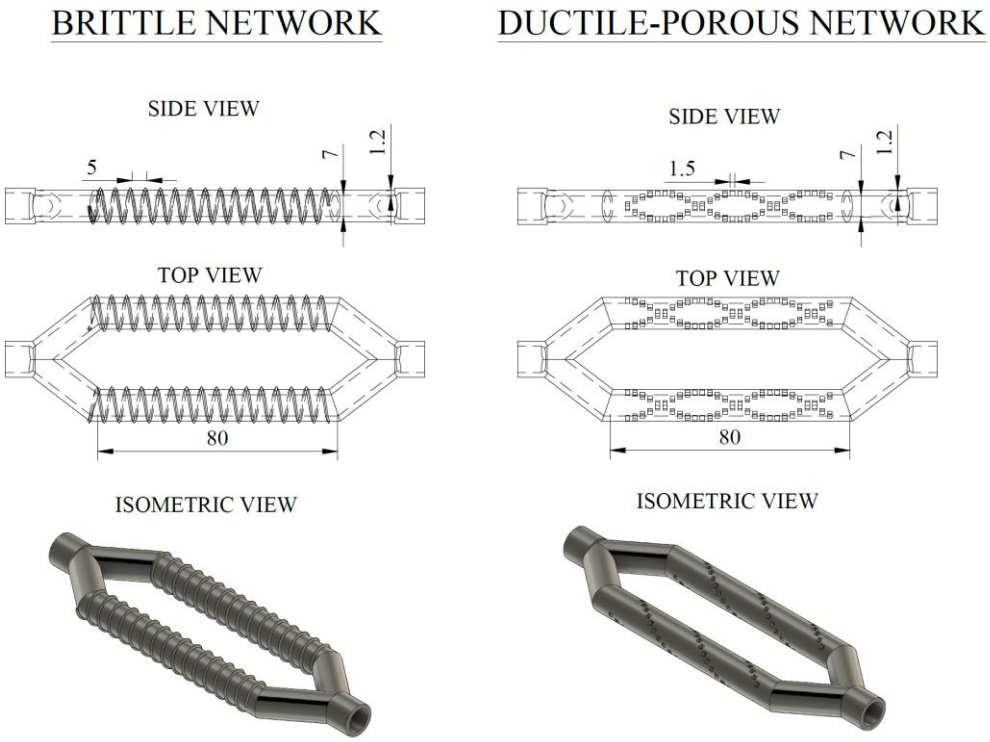

Figure 2. Types of healing agent release mechanisms (dimensions given in mm).

The printing parameters for the different networks are listed in Table 3 and

Table 4. An Ultimaker 2+ printer (Utrecht, The Netherlands) was used to fabricate the FDM networks using a 0.4 mm brass nozzle, and a FormLabs Form 3+ (Somerville, Massachusetts, USA) was used to fabricate the SLA networks.

Table 3. FDM printing parameters.

Parameter	**B-PLA-FDM**	**DP-PP-FDM**
Layer height (mm)	0.25	0.25
Printing speed (mm/sec)	40	30
Nozzle size (mm)	0.4	0.4
Nozzle temperature (°C)	200	220
Infill (%)	100	100
Fan speed (%)	100	100
Bed plate conditions	Painters tape over a glass build plate heated to 60°C	Polypropylene tape over a glass build plate heated to 80°C

Table 4. SLA printing parameters.

Parameter	**DP-FLX-SLA**
Layer height (mm)	0.1
XY Resolution (mm)	0.025
Laser Wavelength (nm)	405
Layer Spot Size (mm)	0.085
Curing Temperature (°C)	60
Curing Time (min)	10

3.3. Mechanical testing procedure for self-healing prisms and their non-destructive evaluation

Mechanical loading: After two weeks of curing, the prisms were loaded in 3-point bending with a span of 190 mm using a universal loading frame with displacement control at 0.05 mm/min until a targeted crack mouth opening displacement (CMOD) of approximately 300 µm was reached. If the CMOD began increasing at an unstable rate, loading was manually terminated to prevent the unreinforced samples from breaking in two parts; at times this resulted in final crack values beyond 300 µm. CMOD was measured by using digital image correlation (DIC), and the final crack width was confirmed by optical microscopy after loading by taking the average of 15 measurements along the crack mouth. Load regains are defined here as the ratio of the healed peak loading and the original peak loading, and stiffness regains are defined as the ratio of the healed stiffness and the original stiffness of the sample. The fracture energy, a concrete fracture mechanics parameter that describes the ability to resist crack propagation, is calculated according to the RILEM TC50-FMC protocol by dividing the work done to perform the fracture process (area under the force-displacement curve until complete failure) by the fractured zone area (width of the beam multiplied by height of the beam without the notch) [19]. As samples were not loaded until complete failure for this work, the fracture energy until peak load, or $G_{F,\,Peak}$, is presented instead.

Digital image correlation (DIC): To prepare the concrete surface for DIC, the back faces of the prisms were painted white with a black random speckle pattern of 1 mm diameter (Figure 3). During testing, two high-resolution cameras were placed facing the painted surface of the prism, and set at a stereo angle of 30°. Vic-Snap software was used for simultaneous image capturing during loading, and the images were post-processed using Vic-3D 8. The subset size was set to 21 pixels and a step size was set to 7 pixels. A Lagrange formulation was applied to calculate the strain.

Acoustic emission (AE): Two acoustic emission sensors were placed on the opposite face from the DIC paint of the prism, with a distance of 180 mm. The probes had a resonant frequency response at 150 kHz and recorded the damage-emitted signals pre-amplified by 40 dB. An amplitude threshold was set at 35 dB to eliminate the ambient noise and the frequency bandwidth was fixed from 20 kHz to 1 MHz. The waveforms were recorded with a sampling rate of 1 Megasample per second (Msps). The DiSP-24 monitoring device was equipped with a PCI/DSP-4 data acquisition board and PowerPAC software provided by Physical Acoustics. A pencil lead breakage test was done before and after any mechanical loading, following the Hsu-Nielsen protocol [20]. The AE hits induced by breaking the pencil lead can show the sound, damaged and healed states by comparing the change of the hits' amplitude.

Ultrasonic pulse velocity (UPV): The ultrasonic pulse velocity of the uncracked, cracked and healed samples was calculated by measuring the transit time of ultrasonic pulses through the beam using the Controls PULSONIC portable device, in accordance with ASTM C597. The transmitter was placed on the side of the prism as shown in Figure 3 and the receiver was placed on the opposite side, so that the transmitted pulses travel across the beam's length. The pulse had a magnitude of 2500 V and frequency of 54 kHz, and the transmitted signal was recorded in a sampling rate of 10 MHz. The transit time (Δt in s) was measured and the

ultrasonic pulse velocity (UPV in m/s) was calculated using a wave propagation distance (Δx) of 0.22 m. This process was repeated before and after each loading cycle.

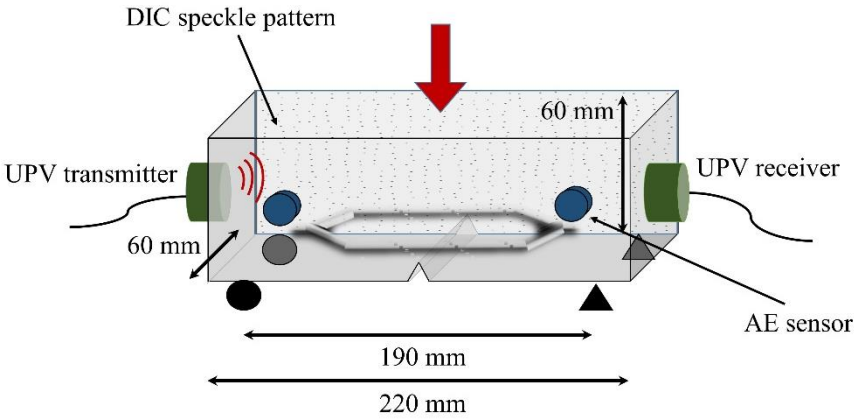

Figure 3. Experimental set-up with DIC speckle pattern on the back of the prism, two AE sensors (blue) on the front of the prism and UPV transmitter/receiver placed at the ends of the prism (green).

Supplying the healing agent: HA FLEX SLV AF, a 1-component polyurethane injection resin (GCP Applied Technologies, Belgium) was chosen for this work due to its success as a healing agent in previous self-healing studies, particularly for its low viscosity (200 mPas at 25°C) to facilitate pumping and its performance in terms of mechanical load regain (155-215% reported in [21]). After loading, the networks were flushed with hot water to prime the cracks to allow the polyurethane to polymerize in a shorter time. The polyurethane was then injected into the networks and pressurized up to 6 bar, and subsequently flushed out with pressurized air to provide a clear passage for future healing cycles. If polyurethane could no longer be pumped through and the passages would be blocked, further loading cycles would not be pursued. An overview of the experimental procedure is given in Figure 4.

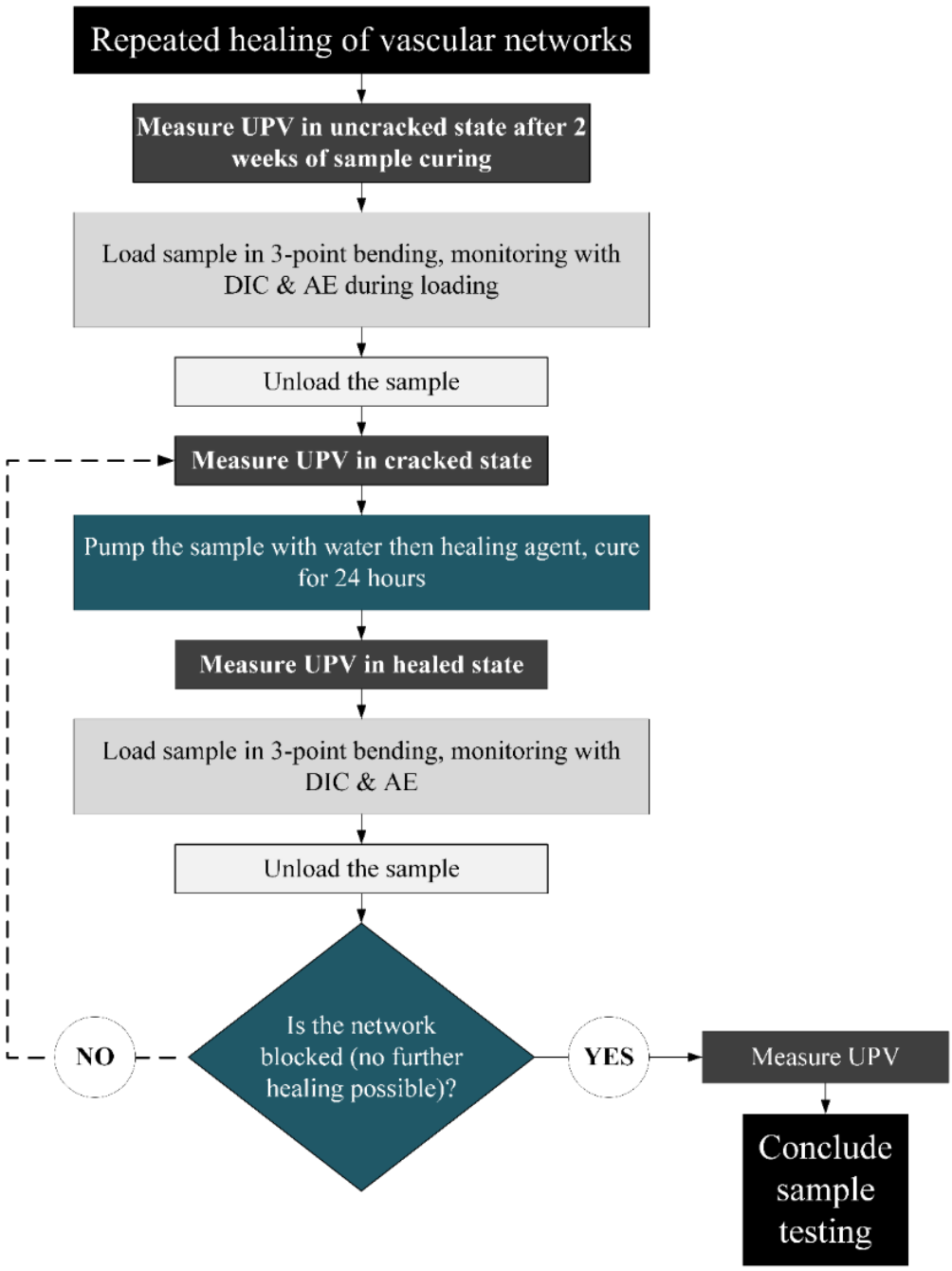

Figure 4. Experimental procedure of repeated healing for vascular networks while monitoring using non-destructive techniques.

Visualization using computed tomography: An additional series of samples were cast and cracked to visualize the internal microstructure of embedded vasculature in concrete using X-ray computed tomography (CT) at the Helmholtz Institute Freiberg for Resource Technology with a CoreTom (XRE–Tescan, Ghent, Belgium) CT scanner. As smaller specimens allow higher image resolution, a separate series of samples were cast with an embedded single tube at the center (instead of a branched network) of 40 x 40 x 160 mm^3 prisms using the mix procedure, concrete cover and network materials previously described, as well as the same curing regime and cracking procedure described in the previous section. The samples were scanned using a 0.5 mm copper filter mounted at the source, a 20 µm voxel size and an X-ray energy of 180 kV. Reconstructions of the projections were done using a 3D reconstruction algorithm in the software Panthera 1.0 (XRE–Tescan, Ghent, Belgium), and filtering of the

images was done using ImageJ. Images of cracked samples prior to any healing action are reported in this study.

4. Results and discussion

Mechanical regain after multiple healing cycles and indications of debonding: The load and stiffness regain for each sample type is summarized in Figure 5. Remarkably, the first cycle for the DP-FLX-SLA networks did not exhibit much load nor stiffness regain, and it substantially increased in the second cycle. Upon microscopic inspection of an unused SLA network, it was found that some of the pores were not fully open because of the SLA resin being not entirely flushed out during post-processing, which could not be seen with an unaided eye but is clearly evident under a microscope (Figure 6). This could explain the overall low healing performance for this network type. Additionally, the increase in healing efficiency for the second healing cycle compared to the first is indicative of additional debonding and flexing of the network, as pores further away from the crack were available to help supply the healing agent. The DP-PP-FDM networks performed the best in terms of load and stiffness regain for the first cycle, achieving averages of 56% and 91%, respectively (with ceiling values of 83.3 and 152%). All network types showed consistent load regain for the second cycle of healing, ranging between 38-44%.

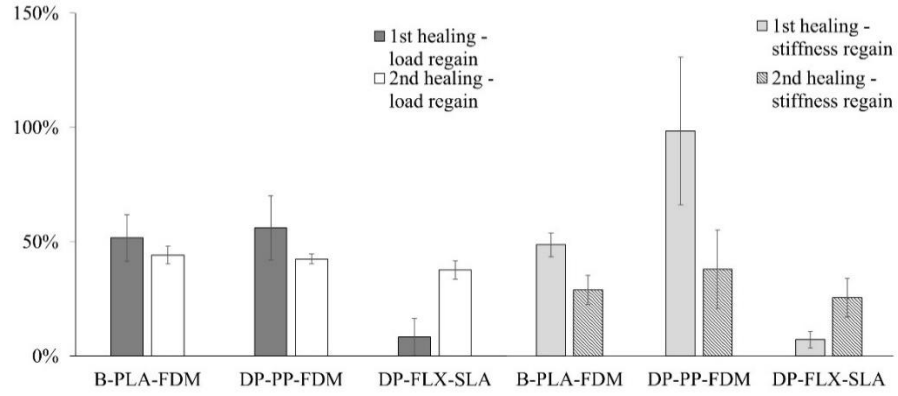

Figure 5. Load and stiffness regain after 2 cycles of healing; an increase in healing efficiency is noted for the DP-FLX-SLA series between its first and second healing cycles. Error bars indicate standard deviation of three specimens.

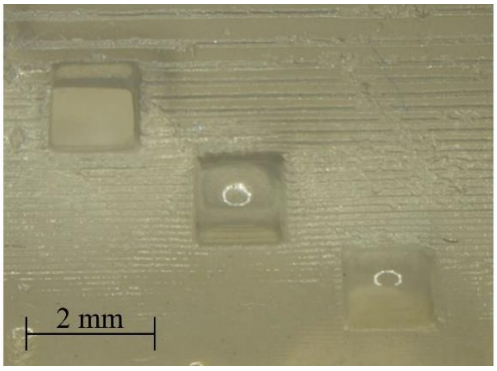

Figure 6. Microscopic image of the midspan of a DP-FLX-SLA network, where some of the pores are only partially open. Scale bar manually inserted after image acquisition for reference.

Impact of networks on structural performance: The average flexural strength of the self-healing specimens and their performance compared to the reference is given in Table 5. While

the DP-FLX-SLA networks showed relatively low healing after the first loading cycle, their presence in fact significantly increased the flexural strength of the prisms in the first loading relative to the REF series and the networks were effectively acting as reinforcement, similar to the PLA self-healing networks used in [9]. A small increase in flexural strength for the B-PLA-FDM networks is noted and expected, as PLA's bending strength is higher than that of concrete, yet the network is fabricated by 3D printing in such a way that the printed layers are parallel to the crack plane and thus will fracture more easily. A significant reduction in flexural strength of 19.3% is noted for the DP-PP-FDM networks.

Table 5. Flexural strength of the self-healing specimens and their performance compared to the reference (average values of three samples).

	Flexural strength (MPa)	**Difference relative to REF**	**Coefficient of variation**
B-PLA-FDM	3.54	2.0%	14.1%
DP-PP-FDM	2.80	-19.3%	23.1%
DP-FLX-SLA	3.88	11.6%	6.6%
REF (no network)	3.47	N/A	17.8%

Gelatin, which was used to seal the pores of the DP networks during the casting process, potentially strengthened localized regions across those networks. Gelatin has been previously used to externally reduce plastic shrinkage in concrete [22], and has shown that its presence in concrete mixtures can help increase its mechanical performance [23], [24]. This could explain the increase for the DP-FLX-SLA networks, however the large negative impact on the flexural strength for the DP-PP-FDM networks (as gelatin was also used for this series) where an increase is expected warrants further discussion. PP is a chemically and thermally stable material, and is therefore unlikely that the heat of hydration and the high pH environment of fresh concrete would deteriorate its mechanical properties. Its weak performance might be due to flaws in the manufacturing of the 3D printed part. To investigate this further, CT images were used to visualize the networks embedded in concrete.

The fracture energy of each network type is compared to the REF series in Table 6. Similar to the flexural strength results, the DP-PP-FDM networks have the largest amount of variation as well as the least amount of fracture energy compared to the other two network types. This is expected given the low peak loading of the DP-PP-FDM networks relative to the other samples, and they had overall lower crack openings (see further in the discussion and within Figure 8). DP-FLX-SLA networks experienced higher loads and displacements, accounting for their higher fracture energy. This high amount of fracture energy of the DP-FLX-SLA networks could also explain the unique cracking patterns that are seen later in the DIC analysis (Figure 12). While the FLEX 80A material has a relatively lower tensile strength compared to the other polymers investigated (9 MPa versus 14 MPa for PP and 37 for PLA), it is possible that it exhibits higher ductility and toughness to resist crack propagation; its ability to deform and absorb energy before failure could contribute to the higher loads that were experienced by the DP-FLX-SLA samples.

Table 6. Comparison of fracture energy (average values of three samples).

	$G_{F,\,Peak}$ (N/m)	**Difference relative to REF**	**Coefficient of variation**
B-PLA-FDM	267	36.6%	8.90%
DP-PP-FDM	227	16.5%	26.3%
DP-FLX-SLA	286	47.2%	15.8%
REF (no network)	195	N/A	4.80%

Measuring damage and healing efficiency using UPV and pencil lead breaks: The UPV measurements are summarized in Figure 7. With the exception of DP-FLX-SLA-3, all samples indicated a UPV recovery between 20-68% after one cycle of healing. DP-FLX-SLA samples had the lowest UPV recovery and mechanical load regain, with an average of 24% UPV recovery after one healing cycle compared to 43% and 45% for DP-PP-FDM and B-PLA-FDM, respectively. After the second crack was generated, there was an overall decrease in UPV recovery for each network type. However, in the case of DP-PP-FDM-1, there was an improvement in UPV recovery in the second healing cycle which exceeded the first healing cycle (4365 m/s compared to 4335 m/s), indicating debonding further away from the crack location. Note that for DP-FLX-SLA-2, there is no second healing present as the channels were blocked and could no longer proceed with further healing and loading cycles.

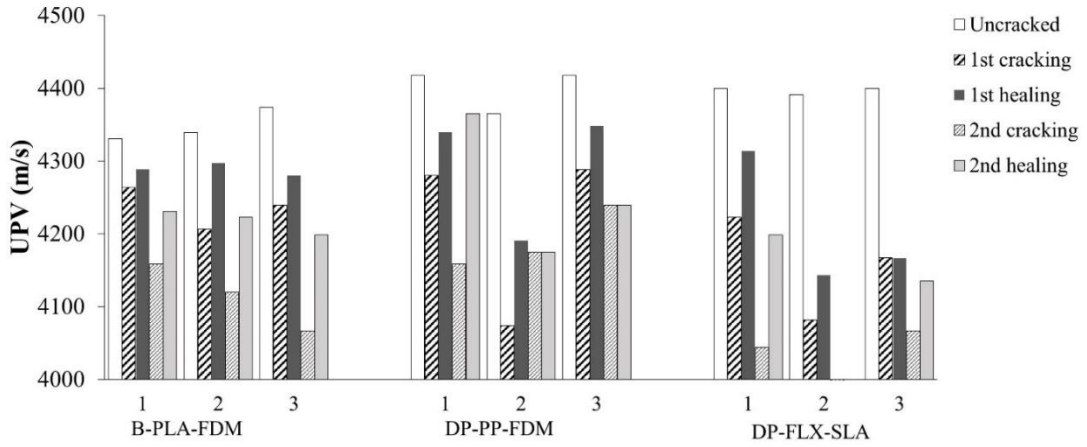

Figure 7. UPV measurements during their uncracked, cracked, and healed states (where 1, 2, and 3 represent the replicate per each series).

In addition to UPV, the amplitudes from the pencil lead breakage test were used to assess the damage of the samples experienced after cracking. Figure 8 assesses each sample with a network in their uncracked and cracked states, in terms of reduction in UPV and amplitude of the pencil lead breaks in relation to the surface crack width (measured by microscopy) at the end of the first loading test. While both measurements exhibit a decreasing linear trend, a stronger correlation is present for the pencil lead breaks as the triggering occurred in close proximity to the acoustic emission sensor, and thus is a more accurate indicator for damage compared to UPV measurements.

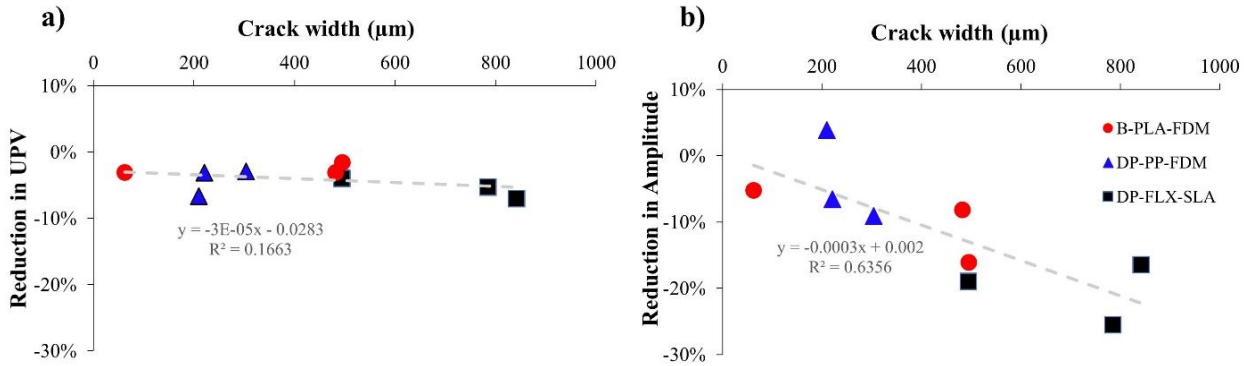

Figure 8. Percent reduction in a) wave velocity (UPV) and b) amplitude of pencil lead breaks versus initial surface crack widths after the first unloading.

Characterization of load-response and crack detection using AE and DIC: The load response and crack detection could be evaluated by coupling acoustic emission and DIC information. In general, less acoustic emission events are expected in ductile materials with progressive crack opening, while a large number of AE events are generated through rapid crack propagation in brittle materials. The total energy emitted from each sample series is shown in Figure 9. It is noted that the REF series exhibits a significantly larger amount of energy overall, with the DP-FLX-SLA series having the second highest amount. From this, each of the network types contributes some amount of ductile behavior to the concrete matrix. This is further confirmed via DIC by characterizing the cracking behavior using the strain profiles, which were calculated along the perimeter of the crack for each sample (Figure 10).

A correlation between Table 6 and Figure 9 is noted for samples containing an embedded network. The REF series does not correlate, as a much higher amount of cumulative energy is seen for the reference samples since they had a sudden and complete failure at the end of their first test (the samples broke completely in two).

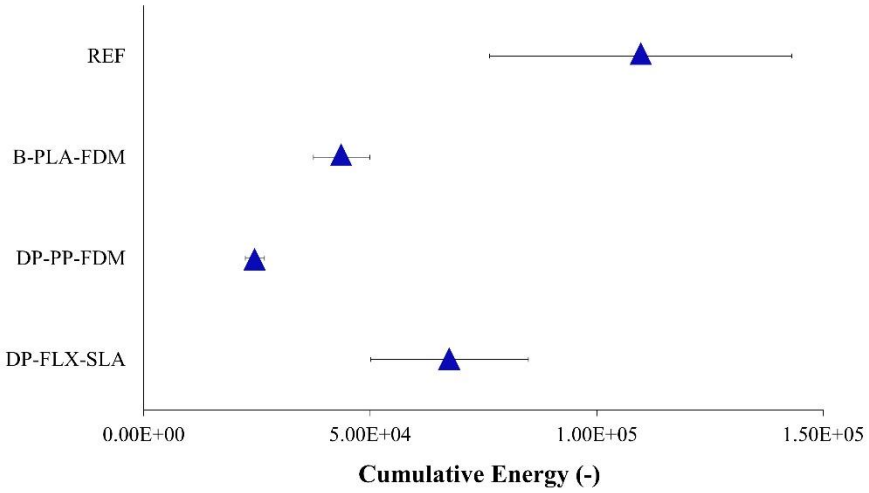

Figure 9. Cumulative acoustic emission energy emitted at the end of the first loading cycle; error bars represent the standard deviation of three specimens.

A series of points were selected in a line following the perimeter of the crack formations. As shown in Figure 11, Line Y represents point locations starting from the base of the crack and going upwards to the tip, then back down along the crack to the base on the other side. The legend of Figure 10 indicates the strains experienced at different loading values during the loading cycle. The DP-PP-FDM series underwent more progressive crack opening, consistent with ductile loading response. Conversely, the B-PLA-FDM, DP-FLX-SLA and REF series had similar strains for the majority of the testing time and only at the end of the loading cycle there was a sharp increase in strain around the crack area, indicating sudden brittle fracture.

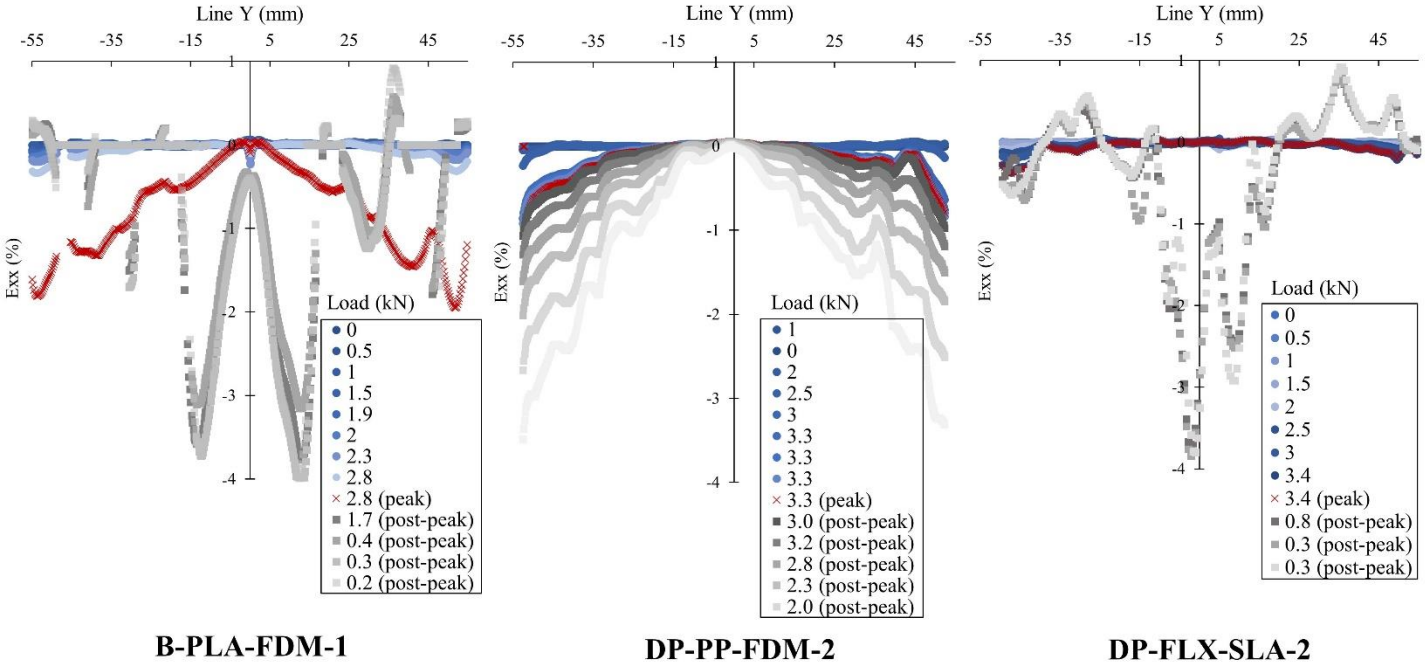

Figure 10. Crack profile strains at different points during the loading cycle.

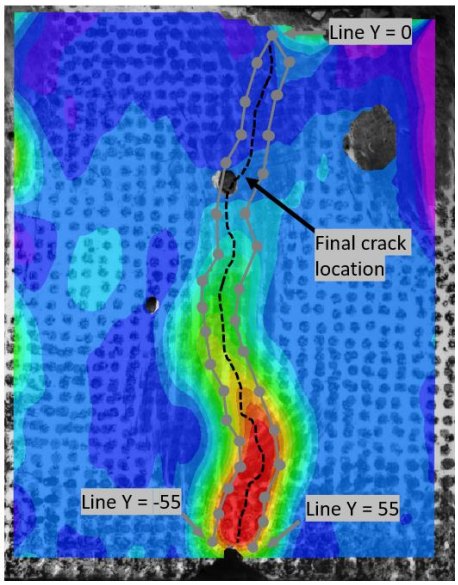

Figure 11. Visual description of the Line Y crack profile strains.

DIC images at different points along the loading regime are given in Figure 12, which includes one representative sample per series as well as their corresponding energy, force (standardized for comparison), and crack opening plots. Since a triangular notch was included in all specimens in order to control the crack pattern and location, straight vertical crack patterns originated from the notch tip for all REF, B-PLA-FDM and DP-PP-FDM samples as intended, however, there were consistently more tortuous and complex cracking patterns

noted for the DP-FLX-SLA samples. The smooth surface of the SLA networks as well as their lack of stiffness could account for their complex crack formation.

In agreement with Figure 10, the appearance of a fully formed crack occurred in a short period of time towards the end of the test for the B-PLA-FDM and DP-FLX-SLA samples, indicating sudden brittle failure. These two series also exhibit a cluster of energy peaking along with the peak load, which corresponds to a large damage event such as this. Crack formation at the surface occurred more progressively during the loading cycle for DP-PP-FDM samples, which is seen by the AE energy points being more scattered throughout the loading cycle. The PP material appears to negatively affect the performance of the prisms, seen by the reduction in flexural strength and fracture toughness compared to the reference samples, and accelerates the crack formation as seen via DIC.

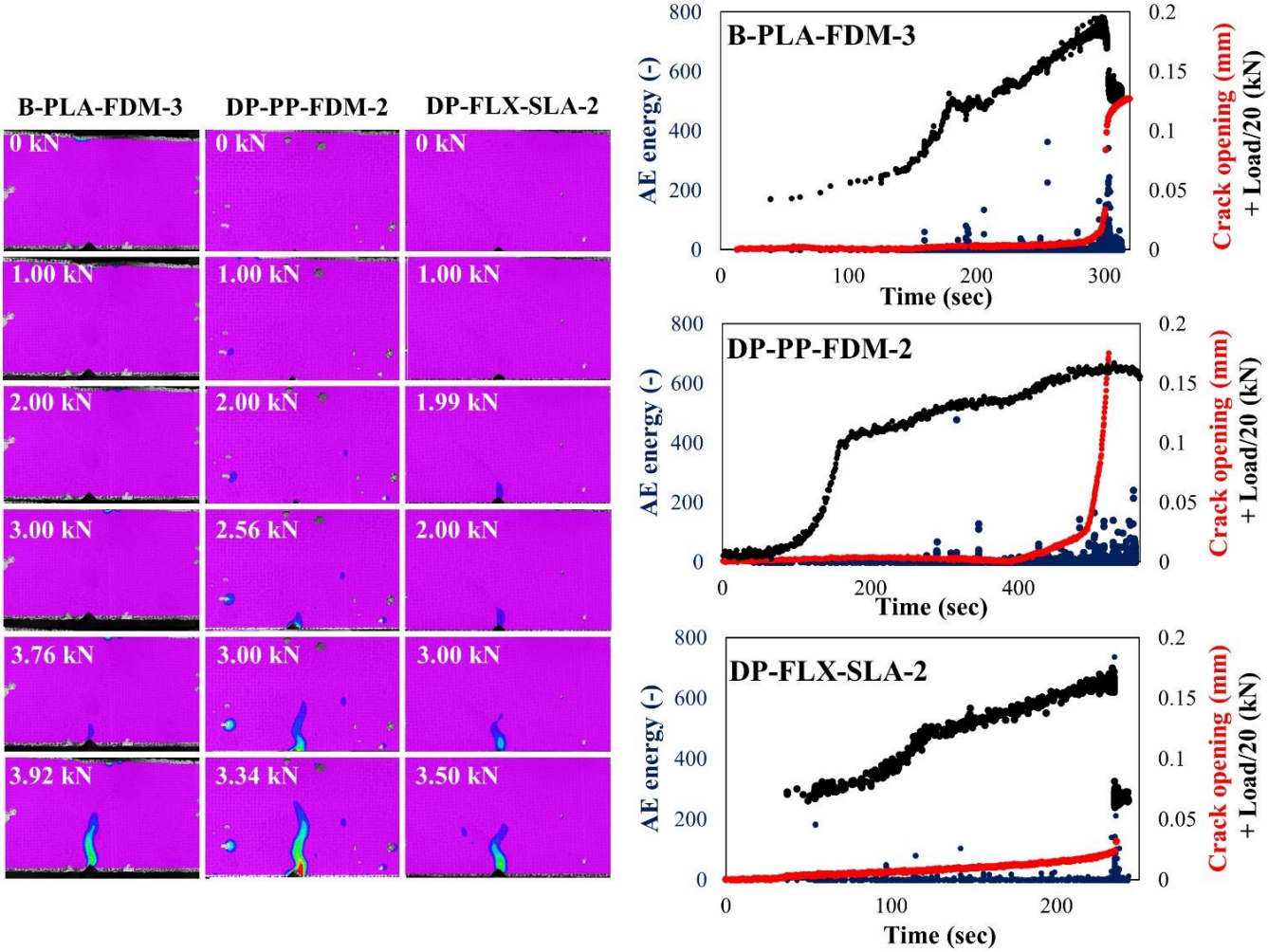

Figure 12. DIC images of representative samples with their corresponding energy, force, and crack opening plots.

Throughout subsequent healing cycles the DIC images also indicated that cracks formed and reopened at the same location for all samples, rather than generating a new crack, thus confirming the flexible nature of the chosen polyurethane healing agent.

AE has been previously used to assess debonding phenomena by evaluating the wave rise time (RT) and average frequency (AF) distributions, where a simultaneous increase in RT and decrease in AF generally indicates shear-dominated behavior [25], [26]. RT-AF plots are shown in Figure 13 and correlated with crack opening of the sample over time. For the B-PLA-FDM and DP-PP-FDM samples, this simultaneous increase in RT and decrease in AF occurred at higher crack openings of approximately 0.075 mm, while this occurred at approximately 0.025 mm for the DP-FLX-SLA sample in Figure 13. This is expected, as the stereolithography printing material has a smoother surface relative to the FDM printed parts and lacks the layer lines that would promote bonding between the network and the surrounding cementitious matrix. In the next section, CT images indicate a larger gap formation relative to the other samples surrounding the DP-FLX-SLA network, which is due to debonding.

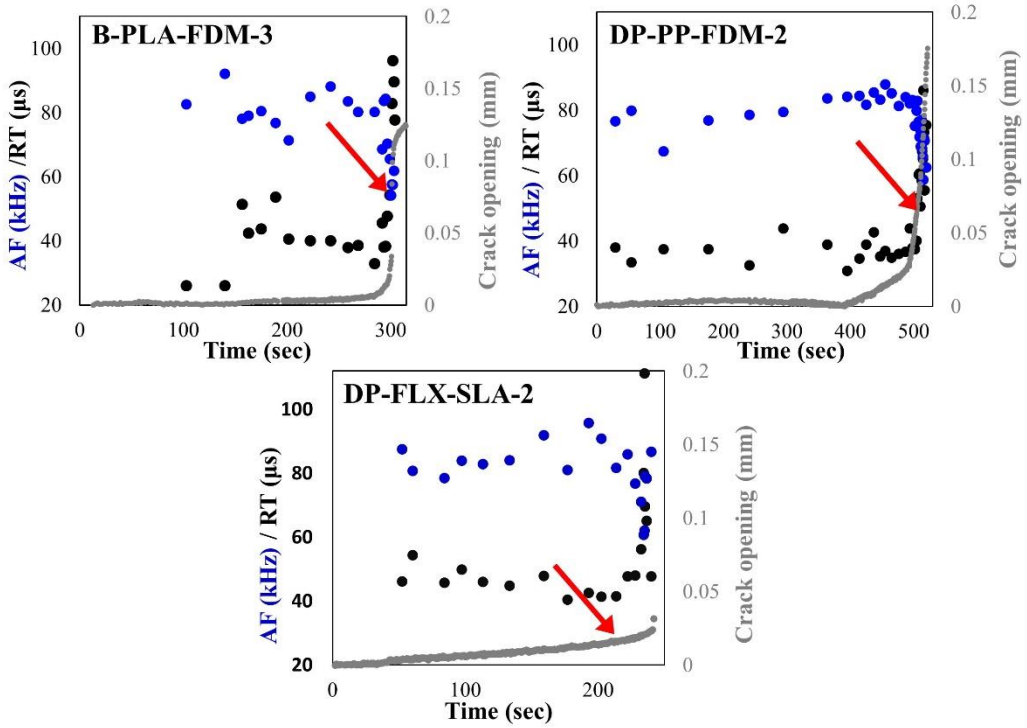

Figure 13. RT-AF plots for representative samples at different stages during the first loading; arrows indicate crack opening at which there was a simultaneous increase in RT and decrease in AF.

Microstructural characterization of potential network wall materials using CT: Representative images of the different sample types within 10 mm of the cracked zones are presented in Figure 14. Arrows point to manufacturing flaws, despite extensive preliminary testing done to determine the printing parameters to avoid defects. For the brittle PLA network (Figure 14a), especially conservative 3D printing slicer settings were used such as a slower printing speed and a larger wall thickness (including 4 perimeter lines to reduce permeability), yet the cross section of the network does not have a 100% infill as originally intended, resulting in an inaccuracy of the 3D print. The quality is thus not sufficient to prevent concrete seepage in areas where the network should be impermeable.

A lack of interlayer adhesion for polypropylene filament is evident in Figure 14b, which allowed cementitious slurry to seep in between the layers. This phenomenon likely accounts for the poor mechanical behavior of the DP-PP-FDM samples relative to the REF samples, and promoted the progressive crack opening seen in the DIC analysis. The inconsistent printing of this material could also account for the large variation in the mechanical results

previously discussed. PP filament is known to have poor adhesion during printing and was printed at higher nozzle temperatures compared to PLA, however an even higher temperature would help with interlayer adhesion to improve the printing quality.

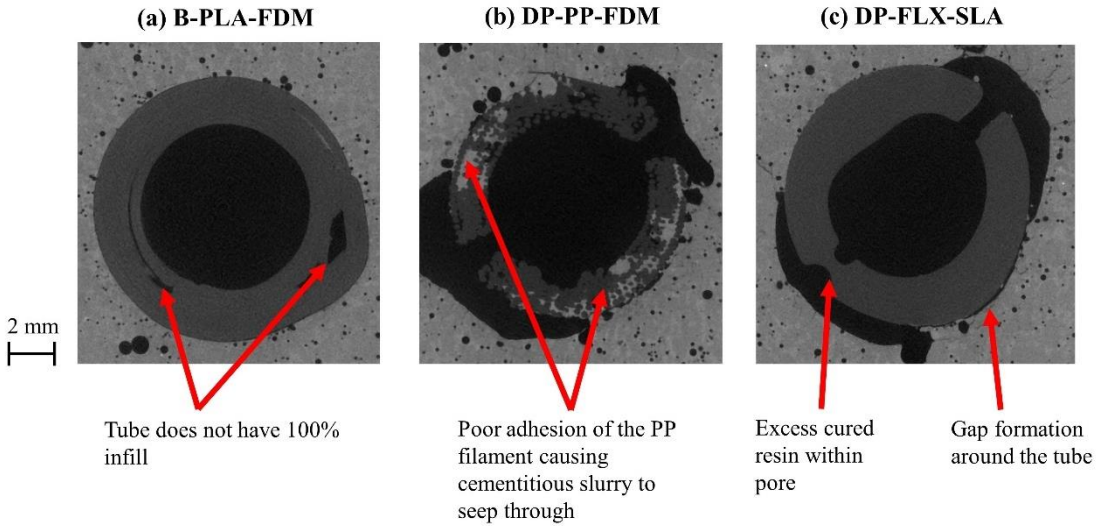

Figure 14. CT images of a) B-PLA-FDM, b) DP-PP-FDM and c) DP-FLX-SLA specimens.

Figure 14c shows the excess resin that partially blocked some of the pores in the DP-FLX-SLA samples (consistent with Figure 6), highlighting the need for an additional post processing step for resin-based printing of porous vascular networks. A noticeable gap formation (having a smaller thickness than the gelatin layer) around the network is visible for the DP network series, and is less prominent for the brittle network series. In both Figure 14b and Figure 14c, the gelatin that was present to block the pores during casting appears to have worked effectively, as there is no cementitious slurry present at those locations.

Given the lack of standards in additive manufacturing, extensive preparation was done prior to producing the 3D printed parts; however, this was not sufficient to produce parts without flaws affecting their structural integrity. Further preliminary testing is needed and standardized 3D printing practices are required to produce precise parts. Standard tube shapes can be more efficiently produced for large-scale uses by traditional extrusion or injection molding procedure, and thus 3D printing is recommended to be more suitable for complex junction parts of vascular networks (where it is difficult to produce via traditional methods) or for prototyping purposes only.

5. Conclusions

In this work, different healing agent release mechanisms (a brittle network and two types of ductile-porous networks) are evaluated in terms of their load-response behavior and self-healing efficiency using AE, UPV, and DIC. Additional CT characterization was used to visualize the embedded tubes within cementitious prisms. The main conclusions are summarized as follows:

- The increase in healing efficiency in terms of load and stiffness regain in the second loading cycle for the SLA-printed networks confirms that the debonding aspect of the ductile-porous network's healing agent release mechanism works as intended.
- Characterization of the brittle response of the brittle networks and ductile response with progressive cracking in the newly developed ductile-porous networks is done via AE and DIC.

- Debonding of both ductile-porous networks can be detected at various times during crack opening by investigating AF/RT AE features.
- Inherent flexibility attributed to the networks produced by SLA caused unique crack patterns to form, instead of the controlled straight cracks seen with all other sample types.
- Healing and crack detection using DIC coupled with AE can verify debonding presence as well as when a healing agent elastically deforms.
- UPV and pencil lead breaks both correlate in terms of measuring damage due to cracking.
- While stereolithography printing allows for more flexible materials to be used, a main drawback is the extensive post-processing required to minimize flaws in production. 3D printing vascular networks works best for prototyping lab-scale systems, however for scaling up, without standard practices for AM and due to its overall longer production time, existing methods such as pipe extrusion or injection molding are both more accurate and more cost efficient to produce linear parts, while only complex branched parts are made via AM. This combination of fabrication methods is promising for future large-scale vascular network production.

6. Acknowledgments

This work acknowledges funding from the SMARTINCS project. This project has received funding from the European Union's Horizon 2020 research and innovation programme under the Marie Skłodowska-Curie grant agreement no. 860006. CT results were granted via the EXCITE network, which received funding from the European Union's Horizon 2020 research and innovation programme under grant agreement no. 101005611. This work also acknowledges Leverhulme Trust ECF-2022-235.

7. References

[1] V. Cappellesso *et al.*, "A review of the efficiency of self-healing concrete technologies for durable and sustainable concrete under realistic conditions," *Int. Mater. Rev.*, pp. 1–48, 2023, doi: 10.1080/09506608.2022.2145747.

[2] C. Dry, "Matrix cracking repair and filling using active and passive modes for smart timed release of chemicals from fibers into cement matrices," *Smart Mater. Struct.*, vol. 3, no. 2, pp. 118–123, 1994, doi: 10.1088/0964-1726/3/2/006.

[3] R. Davies, A. Jefferson, R. Lark, and D. Gardner, "A novel 2D vascular network in cementitious materials," *Concr. - Innov. Des. fib Symp. Proc.*, pp. 249–250, 2015.

[4] Z. Li, L. R. de Souza, C. Litina, A. E. Markaki, and A. Al-Tabbaa, "Feasibility of Using 3D Printed Polyvinyl Alcohol (PVA) for Creating Self-Healing Vascular Tunnels in Cement System," *Materials (Basel).*, 2019, doi: 10.3390/ma12233872.

[5] B. L. Freeman and T. Jefferson, "The simulation of transport processes in cementitious materials with embedded healing systems," *Int. J. Numer. Anal. Methods Geomech.*, vol. 44, no. 2, pp. 293–326, 2020, doi: 10.1002/nag.3017.

[6] T. Selvarajoo, R. E. Davies, B. Freeman, and A. Jefferson, "Mechanical Response of a Vascular Self-Healing Cementitious Material System Under Varying Loading Conditions." *Constr. Build. Mater.*, vol. 254, 2020, doi: 10.1016/j.conbuildmat.2020.119245.

[7] T. Selvarajoo, R. E. Davies, D. R. Gardner, B. L. Freeman, and A. D. Jefferson, "Characterisation of a vascular self-healing cementitious material system : Flow and curing properties," *Constr. Build. Mater.*, vol. 245, p. 118332, 2020, doi: 10.1016/j.conbuildmat.2020.118332.

[8] C. De Nardi, D. Gardner, and A. D. Jefferson, "Development of 3D Printed Networks in Self-Healing Concrete," *Materials (Basel).*, 2020, doi: 10.3390/ma13061328.

[9] Z. Li, L. R. De Souza, C. Litina, A. E. Markaki, and A. Al-tabbaa, "A novel biomimetic design of a 3D vascular structure for self-healing in cementitious materials using Murray ' s law," *Mater. Des.*, vol. 190, p. 108572, 2020, doi: 10.1016/j.matdes.2020.108572.

[10] C. De Nardi *et al.*, "Experimental Investigation of a Novel Formulation of a Cyanoacrylate-Based Adhesive for Self-Healing Concrete Technologies," *Front. Built Environ.*, vol. 7, no. June, pp. 1–15, 2021, doi: 10.3389/fbuil.2021.660562.

[11] Z. Wan, Y. Xu, Y. Zhang, S. He, and B. Šavija, "Mechanical properties and healing efficiency of 3D-printed ABS vascular based self-healing cementitious composite: Experiments and modelling," *Eng. Fract. Mech.*, vol. 267, no. September 2021, 2022, doi: 10.1016/j.engfracmech.2022.108471.

[12] C. De Nardi, D. Gardner, D. Cristofori, L. Ronchin, A. Vavasori, and T. Jefferson, "Advanced 3D printed mini-vascular network for self-healing concrete," *Mater. Des.*, 2023, doi: 10.1016/j.matdes.2023.111939.

[13] Y. Shields, N. De Belie, A. Jefferson, and K. Van Tittelboom, "A review of vascular networks for self-healing applications," *Smart Mater. Struct.*, vol. 30, no. 6, 2021, doi: 10.1088/1361-665X/abf41d.

[14] F. A. Gilabert, K. Van Tittelboom, E. Tsangouri, D. Van Hemelrijck, N. De Belie, and W. Van Paepegem, "Determination of strength and debonding energy of a glass-concrete interface for encapsulation-based self-healing concrete," *Cem. Concr. Compos.*, vol. 79, pp. 76–93, 2017, doi: 10.1016/j.cemconcomp.2017.01.011.

[15] E. Tsangouri *et al.*, "Feasibility study on real-scale , self-healing concrete slab by developing a smart capsules network and assessed by a plethora of advanced monitoring techniques," *Constr. Build. Mater.*, vol. 228, p. 116780, 2019, doi: 10.1016/j.conbuildmat.2019.116780.

[16] P. Minnebo *et al.*, "A novel design of autonomously healed concrete: Towards a vascular healing network," *Materials (Basel).*, vol. 10, no. 1, pp. 1–23, 2017, doi: 10.3390/ma10010049.

[17] E. Tsangouri, C. Van Loo, Y. Shields, N. De Belie, K. Van Tittelboom, and D. G. Aggelis, "Reservoir-Vascular Tubes Network for Self-Healing Concrete: Performance Analysis by Acoustic Emission, Digital Image Correlation and Ultrasound Velocity," *Appl. Sci.*, vol. 12, no. 10, 2022, doi: 10.3390/app12104821.

[18] C. D. Murray, "A relationship between circumference and weight in trees and its bearing on branching angles," *J. Gen. Physiol.*, vol. 10, no. 5, pp. 725–729, 1927, doi: 10.1085/jgp.10.5.725.

[19] A. Hillerborg, "Concrete fracture energy tests performed by 9 laboratories according to a draft RILEM recommendation : Report to RILEM TC50-FMC," 1983.

[20] N. N. Hsu, "Characterization and calibration of acoustic emission sensors.," *Mater. Eval.*, vol. 39, 1981.

[21] Y. Shields, T. Van Mullem, N. De Belie, and K. Van Tittelboom, "An investigation of suitable healing agents for vascular-based self-healing in cementitious materials," *Sustain.*, vol. 13, no. 23, 2021, doi: 10.3390/su132312948.

[22] D. Snoeck, B. Moerkerke, A. Mignon, and N. De Belie, “In-situ crosslinking of superabsorbent polymers as external curing layer compared to internal curing to mitigate plastic shrinkage,” *Constr. Build. Mater.*, vol. 262, p. 120819, 2020, doi: 10.1016/j.conbuildmat.2020.120819.

[23] A. Bigi, B. Bracci, and S. Panzavolta, “Effect of added gelatin on the properties of calcium phosphate cement,” *Biomaterials*, vol. 25, no. 14, pp. 2893–2899, 2004, doi: 10.1016/j.biomaterials.2003.09.059.

[24] W. V. SRUBAR, S. COOK, M. HUBLER, and J. CAMERON, “Living structural material,” WO2020180914A1, 2020.

[25] D. G. Aggelis, D. V Soulioti, N. Sapouridis, N. M. Barkoula, A. S. Paipetis, and T. E. Matikas, “Acoustic emission characterization of the fracture process in fibre reinforced concrete,” *Constr. Build. Mater.*, vol. 25, no. 11, pp. 4126–4131, 2011, doi: 10.1016/j.conbuildmat.2011.04.049.

[26] E. Tsangouri, H. Ismail, M. De Munck, D. G. Aggelis, and T. Tysmans, “Reveal of Internal , Early-Load Interfacial Debonding on Cement Textile-Reinforced Sandwich Insulated Panels,” *Appl. Sci.*, 2021, doi: 10.3390/app11020879.

Declaration of interests

☒ The authors declare that they have no known competing financial interests or personal relationships that could have appeared to influence the work reported in this paper.

☐ The authors declare the following financial interests/personal relationships which may be considered as potential competing interests:

View publication stats